J. Fluid Mech. (2010), *vol.* 659, *pp.* 43–68.
doi:10.1017/S0022112010002387

Locomotion of a passively flapping flat plate

JIE ZHANG, NAN-SHENG LIU
AND XI-YUN LU†

Department of Modern Mechanics, University of Science and Technology of China,
Hefei, Anhui 230026, China

(Received 12 August 2009; revised 16 April 2010; accepted 16 April 2010;
first published online 28 June 2010)

Locomotion of a passively flapping flat plate has been studied numerically by means of a multiblock lattice Boltzmann method. A flexible plate is modelled by a rigid plate with a torsion spring acting about the pivot at the leading edge of the plate. A dynamic model of this kind is called a lumped-torsional-flexibility model. When the leading edge is forced to heave sinusoidally, the plate pitches passively and propels itself in the horizontal direction as a result of the fluid–plate interaction. We have investigated various aspects of the mechanics behind the behaviour of the flapping plate, including the periodic- and non-periodic-flow states, the spontaneous motion of the plate, vortical structure and how they compare to similar propulsion systems in animals. In the periodic-flow regime, two dynamical responses of the passively pitching plate (forward and backward movements) are observed. Which movement will occur depends only on the frequency ratio F of the natural frequency of the system and the heaving frequency associated with the lumped torsional flexibility. It is found that the plate will select the forward movement when $F > 1$ and the backward movement when $F \leqslant 1$. In the forward-movement regime, analysis of the dynamical behaviours and propulsive properties of the passively pitching plate indicates that the torsional flexibility can remarkably improve the propulsive performance. In addition, four kinds of vortex structures in the near wake are identified, which mainly depend on the forward speed of the plate. Finally the forward movement is compared to the flapping-based locomotion of swimming and flying animals. The results obtained in this study are consistent with the observations and measurements of swimming and flying animals; thus, they may provide physical insights into understanding of the propulsive mechanisms of the flapping wings and fins of animals.

Key words: propulsion, swimming/flying

1. Introduction

A common strategy of flying or swimming animals for locomotion through a fluid is to use appendages such as wings or fins to make flapping and pitching motions (Childress 1981; Alexander 1993; Vogel 1994). Real wings and fins of animals possess flexibility (e.g. Blake 1983; Videler 1993; Brodsky 1994; Wootton 1999; Combes & Daniel 2001, 2003*a*,*b*). The flapping flight or swimming is usually accompanied by the obvious bending of the flexible wings and fins. The instantaneous shape of the wings or the fins has, in turn, a profound influence on the fluid dynamic forces. It has been found that the flexibility may significantly improve the flapping-based locomotion

† Email address for correspondence: xlu@ustc.edu.cn

(e.g. Combes & Daniel 2001; Ishihara, Horie & Denda 2009; Vanella *et al.* 2009). In order to further understand the role of flexibility in the flapping of wings and fins in animal locomotion, it is necessary to carry out relevant studies in detail.

It has been identified that insect wings undergo various modes of deformation during flapping motions, and this may affect many aspects of locomotion. Usually, the deformation of the insect wings during flapping is generated by aerodynamic forces, elastic forces and inertial forces due to the accelerations. The wings have complex structural behaviours which mainly depend on the internal distribution of the compliant components (Wootton 1999). Because the insect wings lack internal muscles, there exist no actuators to realize internal control forces (Wootton *et al.* 2003). Consequently, the wings can be twisted easily to have a passive change in the angle of attack (Ennos 1987) or a passive pitching motion. Combes & Daniel (2003*a*,*b*) have addressed the relationship between venation pattern and wing flexibility by measuring the flexural stiffness of wings and quantifying the wing venation. These behaviours also provide a physical basis for building up a reliable model in experimental and numerical investigations.

The deformations of the insect wing during flapping motion are largely passive and are controlled primarily by their architectural and material properties. Combes & Daniel (2003*a*,*b*) have estimated the flexural stiffness variation in the hawkmoth (*Manduca sexta*) and the dragonfly (*Aeshna multicolor*). They found that flexural stiffness declines sharply from the wing base to the tip, and from the leading edge to the trailing edge, and this variation can be approximated by an exponential decrease. As the high flexibility of wings is mainly concentrated on the narrow-basal and short-root regions, the torsional flexibility may be reasonably assumed to be lumped together and be modelled by an elastic spring (Ishihara *et al.* 2009; Vanella *et al.* 2009). The lumped-torsional-flexibility models have been used to investigate the influence of flexibility of wings on the insect hovering flight. The results obtained have showed that the flexibility can improve aerodynamic performance (Ishihara *et al.* 2009; Vanella *et al.* 2009), which indicates the importance of considering nonlinear resonances for enhancing aerodynamic performance.

On the other hand, flapping-based locomotion has attracted much attention because of the fundamental principles involved and their potential applications. Extensive investigations have been performed experimentally (e.g. Gopalkrishnan *et al.* 1994; Ellington *et al.* 1996; Dickinson, Lehmann & Sane 1999; Triantafyllou, Triantafyllou & Yue 2000; Birch & Dickinson 2001) and numerically (e.g. Liu *et al.* 1998; Wang 2000; Ramamurit & Sandberg 2002; Sun & Tang 2002; Wang, Birch & Dickinson 2004; Wang 2005; Gao & Lu 2008). Much has been studied in detail in these works: the leading-edge vortex which induces high lift due to the delayed stall, the lift enhancement due to the rotational effect and the wake capture over a flapping insect wing, the reverse von Kármán vortex street which generates thrust for a flapping wing in a uniform flow, etc. However, we would like to point out that in all of these studies the wing was rigid rather than flexible and its motion was prescribed rather than being passive.

When an animal takes a steady free-flight or swims, the thrust generated will balance resistance. Thus, it is desired to deal with the dynamical behaviours relevant to self-propulsion. When a wing or a fin is flapped in one direction, thrust can be generated in the perpendicular direction (von Kármán & Burgers 1935). Based on this idea, some work has been performed to study the dynamics and mechanisms in flapping free-flight. Vandenberghe, Zhang & Childress (2004) and Vandenberghe, Childress & Zhang (2006) experimentally investigated the dynamics of a rigid, symmetric wing that was flapped vertically in a fluid and moved freely in the horizontal direction.

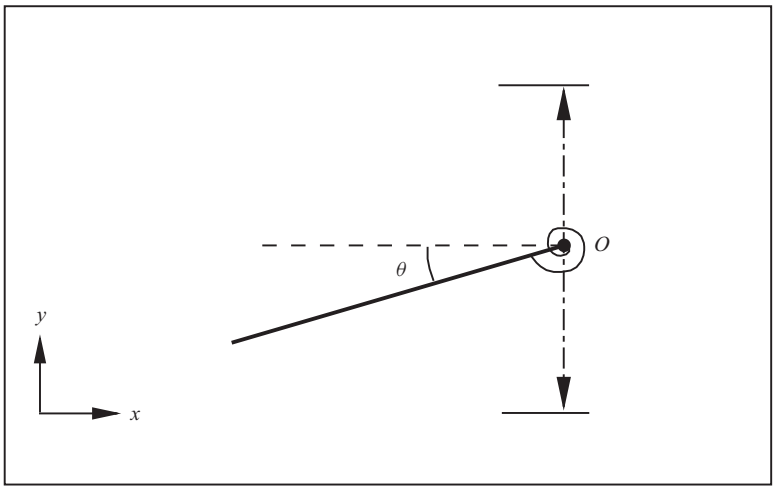

FIGURE 1. Sketch of a simple model for a passively pitching flat plate with torsional flexibility. The flexibility of a plate is simulated by a torsion spring at the plate edge pivot O. When the edge is forced to heave vertically sinusoidally, the plate pitches passively and is free to move horizontally. A Cartesian coordinate system (x, y) with the origin at the edge O is used.

They found that above a critical flapping frequency, forward flight arises as the wing accelerates to a terminal state of constant speed. The wing can move in either direction; once the direction is chosen, it does not change. The dynamics of a two-dimensional flapping body in a viscous fluid were investigated numerically by Alben & Shelly (2005) and Lu & Liao (2006). However, these investigations only considered the heaving motion rather than the passively pitching motion caused by the torsional flexibility. Very recently, the dynamics of a heaving foil with passive pitching were investigated experimentally (J. Zhang, private communication, 2008) and numerically (Spagnolie 2008) to understand the role of flexibility in flapping locomotion. However, the various underlying mechanisms and the intrinsic connections to animal locomotion are still not well understood.

In this study, the locomotion of a passively flapping plate is investigated by solving the Navier–Stokes equations using a multiblock lattice Boltzmann method (LBM) (Yu, Mei & Shyy 2002; Peng *et al.* 2006; Gao & Lu 2008). The flexibility of the plate is simulated by a torsion spring acting about the pivot at the leading edge of the plate which is used to allow a passive flapping motion of the plate. The purpose of this study is to achieve a greater understanding of some of the fundamental phenomena involved in this spring-loaded passively flapping plate, including the periodic- and non-periodic-flow states, the spontaneous motion of the plate, the vortical structures and the intrinsic connections to animal locomotion.

This paper is organized as follows. The physical problem and mathematical formulation are described in § 2. The numerical method and validation are given in § 3. Detailed results are discussed in § 4 and concluding remarks are made in § 5.

2. Physical problem and mathematical formulation

To understand the role of flexibility in flapping wings and fins in animal locomotion, a lumped-torsional-flexibility model is built based on the material and structure of real wings/fins. A diagram is shown in figure 1. The flexibility of a plate is modelled by a torsion spring at the leading edge of the plate O. When the edge is forced to

heave sinusoidally in the vertical direction, the plate pitches passively and propels itself in the horizontal direction due to the fluid–plate interaction. We are aware of the limitations of this simple model; nevertheless, we feel that the results obtained from this model will be helpful in physical understanding of the mechanisms of flapping-based locomotion by the animal's flexible wings/fins.

The incompressible Navier–Stokes equations are used to describe the flow dynamics and are given as

$$\frac{\partial \boldsymbol{u}}{\partial t} + \boldsymbol{u}\cdot\nabla\boldsymbol{u} = -\frac{1}{\rho}\nabla p + \frac{\mu}{\rho}\nabla^2\boldsymbol{u}, \tag{2.1}$$

$$\nabla\cdot\boldsymbol{u} = 0, \tag{2.2}$$

where $\boldsymbol{u}$ is the velocity, p the pressure, ρ the density of the fluid and μ the dynamic viscosity.

Based on the model in figure 1, the edge O of the plate is driven sinusoidally in the vertical direction and is described as

$$y_b(t) = -\bar{A}\cos(2\pi f t), \tag{2.3}$$

where $\bar{A}$ and f are the flapping amplitude and frequency, respectively. A flapping Reynolds number is defined as $Re_f = \rho f \bar{A} c/\mu$, where c is the length of the plate, and a frequency Reynolds number is defined as $\beta = \rho f c^2/\mu$ (Alben & Shelly 2005; Lu & Liao 2006). The two Reynolds numbers are related by the equation $Re_f = \beta A$, with the non-dimensional flapping amplitude $A = \bar{A}/c$.

The pitching motion of the plate with a torsion spring is governed by

$$I\frac{\mathrm{d}^2\theta}{\mathrm{d}t^2} = -k\theta + T_r, \tag{2.4}$$

where θ is the pitching angle, k is the spring stiffness and I and T_r are the moment of inertia of the plate and the fluid moment with respect to the edge O. The natural frequency of the oscillating plate system is defined as $f_n = \{1/(2\pi)\}\sqrt{k/I}$.

The horizontal motion of the plate is not specified, but is rather determined by the fluid force through Newton's second law:

$$m\frac{\mathrm{d}^2 x_b}{\mathrm{d}t^2} = F_x, \tag{2.5}$$

where x_b is the horizontal location of the plate, m is the plate mass given by $m = \rho_l c$ where ρ_l is the linear density of the plate and F_x is the horizontal force component due to the pressure and friction forces exerted on the plate by the surrounding fluid. Then, the horizontal speed U_b is calculated by

$$U_b(t) = \frac{\mathrm{d}x_b}{\mathrm{d}t}. \tag{2.6}$$

Finally, we summarize the governing parameters in this problem. Based on the non-dimensionalized analysis, there exist four parameters: the dimensionless flapping amplitude A, the frequency Reynolds number β, the linear density ratio of the plate and the fluid $D = \rho_l/\rho c$ and the frequency ratio of the natural frequency and the flapping frequency $F = f_n/f$, which is related to the plate torsional flexibility (Ishihara *et al.* 2009; Vanella *et al.* 2009). In addition, a movement Reynolds number is defined as $Re_U = \rho U c/\mu$ (Lu & Liao 2006), which is used to characterize the mean horizontal speed U after the plate begins its steady movement.

3. Numerical method and validation

3.1. *Numerical method*

The LBM is an approach to solve fluid dynamics problems by mesoscopic kinetic models. The LBM avoids treating the nonlinear convective term and solving the Poisson equation for the pressure, which are usually needed in conventional numerical schemes based on discretizations of the incompressible Navier–Stokes equations. Some advantages of the LBM include high computational efficiency and low numerical dissipation (Chen & Doolen 1998; Yu *et al.* 2003). Moreover, it is convenient for treating moving bodies (e.g. Aidun, Lu & Ding 1998; Xia *et al.* 2009). In this study, a multiblock LBM technique (Yu *et al.* 2002; Peng *et al.* 2006) is employed to solve our problem. It is described as follows.

3.1.1. *Lattice Boltzmann model*

The lattice Boltzmann equation (LBE) with the single-relaxation-time approximation is written as

$$f_i(\boldsymbol{x}+\boldsymbol{e}_i\Delta t, t+\Delta t) - f_i(\boldsymbol{x}, t) = -\frac{1}{\tau}\left[f_i(\boldsymbol{x}, t) - f_i^{eq}(\boldsymbol{x}, t)\right], \tag{3.1}$$

where τ is the relaxation time, Δt is the time increment and $f_i(\boldsymbol{x}, t)$ is the distribution function for particles with velocity $\boldsymbol{e}_i$ at position $\boldsymbol{x}$ and time t. The LBE is usually solved in the following two steps, i.e. collision and streaming:

$$\tilde{f}_i(\boldsymbol{x}, t+\Delta t) = f_i(\boldsymbol{x}, t) - \frac{1}{\tau}\left[f_i(\boldsymbol{x}, t) - f_i^{eq}(\boldsymbol{x}, t)\right], \tag{3.2}$$

$$f_i(\boldsymbol{x}+\boldsymbol{e}_i\Delta t, t+\Delta t) = \tilde{f}_i(\boldsymbol{x}, t+\Delta t), \tag{3.3}$$

where $\tilde{f}_i$ denotes the post-collision state of the distribution function. The D2Q9 model (Qian, d'Humieres & Lallemand 1992) is used in the present computation, and the equilibrium distribution function f_i^{eq} is defined as

$$f_i^{eq} = \omega_i\rho\left[1 + \frac{\boldsymbol{e}_i\cdot\boldsymbol{u}}{c_s^2} + \frac{\boldsymbol{u}\boldsymbol{u}:(\boldsymbol{e}_i\boldsymbol{e}_i - c_s^2\boldsymbol{I})}{2c_s^4}\right], \tag{3.4}$$

where ω_i is the weighting factor, c_s is the speed of sound and ρ and $\boldsymbol{u}$ are the fluid density and velocity, respectively, which can be obtained by the distribution function:

$$\rho = \sum_i f_i, \tag{3.5}$$

$$\rho\boldsymbol{u} = \sum_i \boldsymbol{e}_i f_i. \tag{3.6}$$

3.1.2. *Boundary conditions*

To treat the boundary conditions on the moving boundaries, an interpolation bounce-back scheme (Lallemand & Luo 2003) is used and a diagram is given in figure 2. The parameter q represents the fraction of an intersected link on the same side of the wall as the fluid node at $\boldsymbol{x}_f$, and is given by $q = |\boldsymbol{x}_f - \boldsymbol{x}_w|/\delta_x$. The distribution function $f_{\bar{i}}(\boldsymbol{x}_f, t)$ of velocity $\boldsymbol{e}_{\bar{i}}$, where $\boldsymbol{e}_{\bar{i}} \equiv -\boldsymbol{e}_i$, can be determined by taking the moving-wall effect into account and is given as

$$\begin{aligned} f_{\bar{i}}(\boldsymbol{x}_f, t) = {} & q(1+2q)f_i(\boldsymbol{x}_f + \boldsymbol{e}_i\Delta t, t) + (1-4q^2)f_i(\boldsymbol{x}_f, t) \\ & - q(1-2q)f_i(\boldsymbol{x}_f - \boldsymbol{e}_i\Delta t, t) + 2\omega_i\rho_w\frac{(\boldsymbol{e}_i\cdot\boldsymbol{u}_w)}{c_s^2}, \qquad q < 1/2, \end{aligned} \tag{3.7}$$

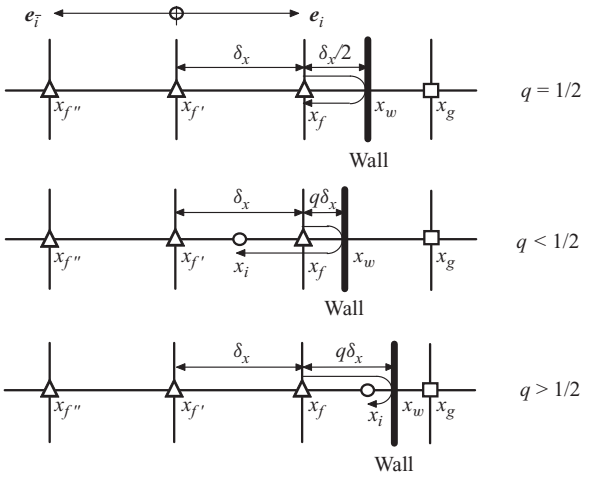

FIGURE 2. Illustration of the boundary conditions for a rigid wall located between two grid sites in the direction of the motion of the particle that is rebounded. The symbol △ represents fluid nodes, ○ the interstitial position of the particle that has rebounded and □ the ghost nodes.

$$f_{\bar{i}}(\boldsymbol{x}_f, t) = \frac{1}{q(2q+1)} f_i(\boldsymbol{x}_f + \boldsymbol{e}_i \Delta t, t) + \frac{(2q-1)}{q} f_{\bar{i}}(\boldsymbol{x}_f - \boldsymbol{e}_i \Delta t, t) - \frac{(2q-1)}{(2q+1)} f_{\bar{i}}(\boldsymbol{x}_f - 2\boldsymbol{e}_i \Delta t, t) + 2\omega_i \rho_w \frac{(\boldsymbol{e}_i \cdot \boldsymbol{u}_w)}{q(2q+1)c_s^2}, \qquad q \geqslant 1/2, \quad (3.8)$$

where $\boldsymbol{u}_w$ is the velocity of the moving wall at position $\boldsymbol{x}_w$ and ρ_w is the fluid density at the wall that can be specified by $\rho_w = \rho(\boldsymbol{x}_f)$ since the flow is nearly incompressible (Yu *et al.* 2003).

Due to the movement of the plate over the lattice, certain fluid nodes will move across the plate from one side to another. When such a fluid node is detected, the distribution function at this node, $\boldsymbol{x}_a$, is reconstructed to be the average of the extrapolated-distribution-function values from a second-order extrapolation scheme over all the possible directions (Fang *et al.* 2002; Connington *et al.* 2009). A possible direction is any direction $\boldsymbol{e}_k$, where both $\boldsymbol{x}_a + \boldsymbol{e}_k \Delta t$ and $\boldsymbol{x}_a + 2\boldsymbol{e}_k \Delta t$ are the fluid nodes (excluding the reconstructed nodes on the same side of the plate as the node $\boldsymbol{x}_a$). The extrapolation is given by

$$f_i(\boldsymbol{x}_a) = \frac{\sum_{k \in S} \{2 f_i(\boldsymbol{x}_a + \boldsymbol{e}_k \Delta t) - f_i(\boldsymbol{x}_a + 2\boldsymbol{e}_k \Delta t)\}}{N_S} \qquad \forall \ i, \quad (3.9)$$

where S is the set of all possible directions and N_S is the number of elements in S. Fang *et al.* (2002) have indicated that the mass is approximately conserved at the boundaries.

In this study, a finite moving computational domain with a sufficiently long section, both upstream and downstream of the plate, is used (Aidun *et al.* 1998; Aidun & Ding 2003). The inlet boundary of the domain, where a zero velocity is taken uniformly, is $30c$ away from the plate edge O, whereas the outlet boundary is $30c$ away from the edge O. The normal derivative of velocity is set to zero at the outlet boundary. Every time the plate moves one lattice unit on the coarse grid in the horizontal direction, the computational domain is shifted, i.e. adding one 'layer' at the inlet and removing one 'layer' at the outlet (Xia *et al.* 2009).

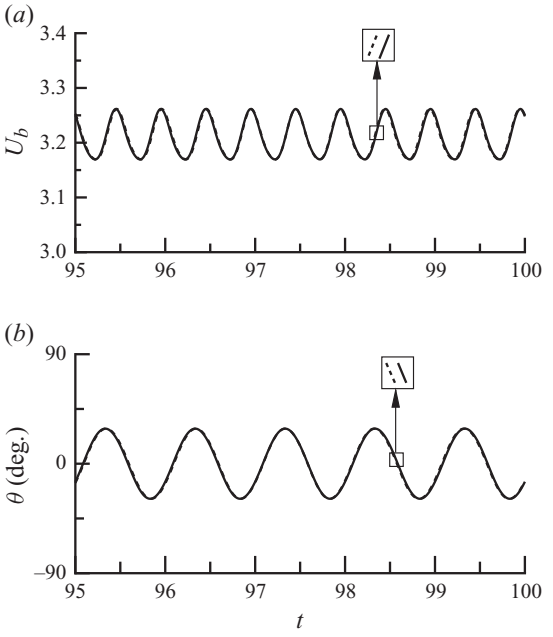

FIGURE 3. Time-dependent (a) horizontal speed $U_b(t)$ and (b) pitching angle $\theta(t)$ calculated under different computational conditions for $F = 1.05$, $\beta = 80$, $A = 0.5$ and $D = 2$. Solid lines: the finest lattice spacing $\Delta x = 0.005c$, time step $\Delta t = 0.0005T$, with T being the flapping period, and computational domain $-30c \leqslant x \leqslant 30c$ and $-15c \leqslant y \leqslant 15c$; dashed lines: $\Delta x = 0.01c$, $\Delta t = 0.001T$ and $-20c \leqslant x \leqslant 20c$ and $-10c \leqslant y \leqslant 10c$.

3.1.3. *Force calculation on plate surface*

The momentum-exchange method is employed to evaluate the fluid force and moment exerted on the plate (Mei *et al.* 2002; Lallemand & Luo 2003; Connington *et al.* 2009). For each link connecting a fluid node to the moving plate, the fluid exerts a force on the plate in that link direction, realized as an instantaneous momentum exchange between the fluid and the plate. Using the terminology of figure 2, the force exerted on the plate along a relevant direction $\boldsymbol{e}_i$ connecting a fluid node at $\boldsymbol{x}_f$ to the position of the wall at $\boldsymbol{x}_w$ is

$$F(\boldsymbol{x}_w, \boldsymbol{e}_i) = \boldsymbol{e}_i(f_i(\boldsymbol{x}_f, t) + f_{\bar{i}}(\boldsymbol{x}_f, t)), \tag{3.10}$$

where $f_{\bar{i}}(\boldsymbol{x}_f, t)$ is computed by (3.7) or (3.8). The total fluid force on the plate is the sum of the forces computed from each relevant link connecting a fluid node to the plate. The total fluid moment on the plate can be obtained using this information (Mei *et al.* 2002; Lallemand & Luo 2003; Connington *et al.* 2009).

3.2. *Validation*

To validate the method, convergence checks have been performed. As a typical case, the time-dependent horizontal speed $U_b(t)$ and pitching angle $\theta(t)$ calculated by different lattice spacings and different sizes of the computational domain are shown in figure 3. The results from these different computations agree well with each other. It is confirmed that the computed results are independent of the lattice spacing and computational domain size. Convergence studies indicate that the LBM method used in our study is second-order accurate in L_∞ and L_2 norms for variables such as the

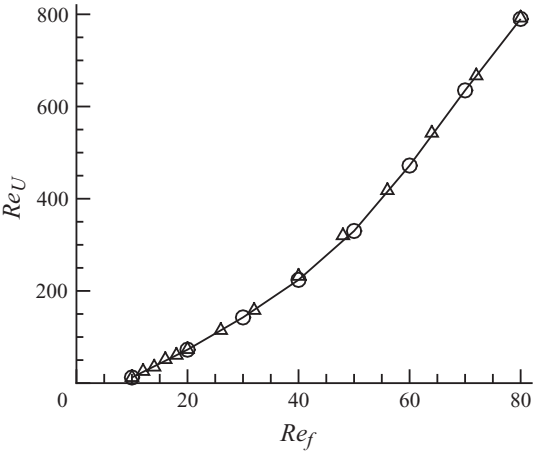

FIGURE 4. Comparison of the present result and previous data (Alben & Shelly 2005) for the forward Reynolds number Re_U versus the flapping Reynolds number Re_f during steady locomotion for flapping flight of an elliptic foil with the thickness ratio 0.1, the flapping amplitude 0.5 and the density ratio 32, where ○ with the solid line denotes the present results and △ the previous data (Alben & Shelly 2005).

plate speed, the pitching angle and the flow velocity. This is consistent with previous convergence checks (e.g. Bouzidi, Firdaouss & Lallemand 2001; Yu *et al.* 2003).

The results given below were calculated on the finer grid and the larger domain. The computational domain is chosen as $-30c \leqslant x \leqslant 30c$ and $-15c \leqslant y \leqslant 15c$, with the finest lattice spacing of $0.005c$ in the region of the plate and the coarsest spacing of $0.04c$ near the top and bottom boundaries. The time step is $0.0005T$, with T being the flapping period. The time-averaged quantities are calculated after elimination of the transition in their time-dependent variations.

To perform quantitative comparison with existing results in the literature, we consider an elliptic foil being flapped vertically within a viscous fluid and moving freely in the horizontal direction which has been well studied experimentally (Vandenberghe *et al.* 2004, 2006) and numerically (Alben & Shelly 2005; Lu & Liao 2006). Actually, this problem corresponds to the limiting case in our current study where the spring stiffness in (2.4) or the natural frequency of the fluid–plate system approaches infinity. Figure 4 shows some typical results of the mean horizontal speed during steady locomotion characterized by Re_U versus the flapping Reynolds number Re_f for an elliptic foil with thickness ratio 0.1, flapping amplitude 0.5 and density ratio 32. Note that this density ratio is different from the linear density ratio used in the present study. It is seen that our calculated results agree well with the numerical data computed by the 'vorticity–streamfunction' formulation of the Navier–Stokes equations (Alben & Shelly 2005).

In addition, the code used here for our current study has been validated carefully in our previous work (e.g. Peng *et al.* 2006; Gao, Tseng & Lu 2007; Gao & Lu 2008). The numerical method has also been applied with success to a wide range of flows such as insect normal hovering flight with ground effect (Gao & Lu 2008), the aerodynamic performance due to forewing and hindwing interaction in gliding dragonfly flight (Zhang & Lu 2009) and the transition from steady to chaotic state for a viscous flow past an inclined flat plate (Zhang, Liu & Lu 2009).

4. Results and discussion

In this section, we present some typical results of the dynamical behaviours and propulsive properties of the passively pitching plate due to the fluid–plate interaction, and we discuss the intrinsic connections of our results to the flapping-based locomotion of swimming and flying animals. Motivated by the measurements of animal locomotion (e.g. Richard 1958; Ellington 1984*a*,*b*; Fish 1993; Drucker & Lauder 2001; Taylor, Nudds & Thomas 2003; Fish 2004), the governing parameters used in this study are chosen as follows: the frequency ratio $F = 0.5$–10, the linear density ratio $D = 0.2$–10, the flapping amplitude $A = 0.2$–1 and the frequency Reynolds number $\beta = 20$–120.

4.1. *Periodic- and non-periodic-flow states*

Based on a series of simulations over a wide range of the parameters, we find that there exist two typical flow states in this fluid–plate interaction system: a periodic- and a non-periodic-flow state. The boundary between these two flow states is determined approximately. The details are discussed below.

To summarize our findings on the two flow states, an overview of the periodic and non-periodic regions in the (F, D) plane is shown in figure 5 for several values of β and A. The non-periodic region (i.e. region I) shrinks somewhat as D increases. Comparing the boundaries shown in figures 5(*a*)–5(*c*) for $\beta = 20$, 80 and 120, we can see that the boundary moves towards the higher frequency ratio with the increase in β. Furthermore, as typically shown in figure 5(*b*), for the boundaries at $A = 0.3$, 0.5 and 0.7, the non-periodic region becomes larger with the increase of A.

To understand the flows in the periodic- and non-periodic-flow regimes, the time-dependent horizontal speed $U_b(t)$ and pitching angle $\theta(t)$ are shown in figure 6 for three typical frequency ratios: $F = 0.7$, 0.95 and 1.05. The corresponding power spectra of $U_b(t)$ and $\theta(t)$, and the instantaneous vortical structures are shown in figure 7. At $F = 0.7$, in the non-periodic-flow region of figure 5(*b*), the non-periodic variations of $U_b(t)$ and $\theta(t)$ in figures 6(*a*) and 6(*b*) are obvious. The power spectra of $U_b(t)$ and $\theta(t)$ are also shown in figure 7(*a*), and the broadband continuous spectrum clearly shows the non-periodic behaviour. The corresponding vortex structures in figure 7(*d*) illustrate the complex non-periodic interactions in the near wake.

As F increases, the flow state switches from the non-periodic to the periodic regime in figure 5. For $F = 0.95$ and 1.05, lying in the periodic-flow region in figure 5(*b*), all the curves of $U_b(t)$ and $\theta(t)$ in figure 6 and their power spectra in figures 7(*b*) and 7(*c*) indicate the periodic behaviour. Although the plate can move freely in the horizontal direction, it does not mean that the net horizontal force is zero at any moment. The force is typically oscillatory, resulting in periodic acceleration and deceleration of the plate. Thus, when the plate has a pitch-up or a pitch-down motion, as typically shown in figure 3, the plate will undergo accelerating and decelerating motions. Therefore, as shown in figures 7(*b*) and 7(*c*), it is reasonable that the primary frequency of $U_b(t)$ corresponding to the peak of the power spectrum is twice that of $\theta(t)$.

Moreover, as the plate moves spontaneously in the horizontal direction, vortex shedding occurs with a reverse von Kármán vortex street exhibited in figures 7(*e*) and 7(*f*). This behaviour is consistent with the experimental and numerical findings for a vertical flapping wing (e.g. Vandenberghe *et al.* 2004; Alben & Shelly 2005; Lu & Liao 2006; Vandenberghe *et al.* 2006). Detailed discussion on the vortex structures in the wake will be given in § 4.4.

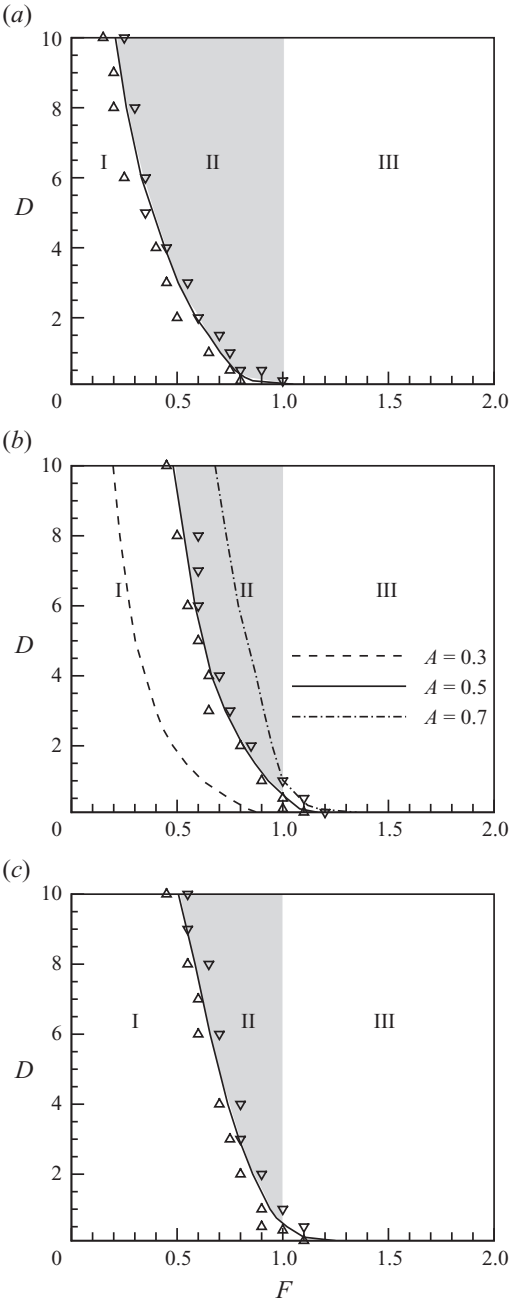

FIGURE 5. Classification of the flow state in the (F, D) plane for different values of β: (a) 20, (b) 80 and (c) 120. Solid line (fitting curve) denotes the boundary between the non-periodic-flow (region I) and periodic-flow (region II with shading for $F \leqslant 1$ and region III for $F > 1$) states at $A = 0.5$, where I is the non-periodic region, II the periodic backward-movement region and III the periodic forward-movement region. Symbols $\triangle$ and $\triangledown$, corresponding to some typical cases calculated here, represent the non-periodic- and periodic-flow states, respectively. The boundaries between the non-periodic and periodic states for $A = 0.3$ (dashed line) and $A = 0.7$ (dashed–dotted line) are also drawn in (b).

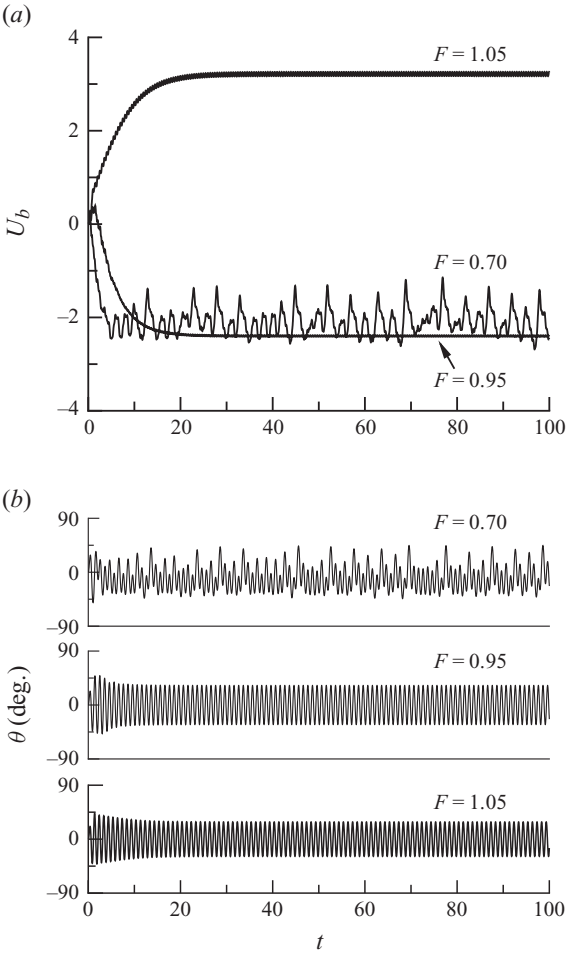

FIGURE 6. Time histories of (a) horizontal speed U_b and (b) passive pitching angle θ at three typical frequency ratios $F = 0.7$, 0.95 and 1.05 for $\beta = 80$, $A = 0.5$ and $D = 2$.

The influence of flapping amplitude A on the boundary between the periodic- and non-periodic-flow regions is given in figure 5(b). To demonstrate the periodic- and non-periodic-flow behaviours, figure 8 shows the time-dependent horizontal speed $U_b(t)$ for $A = 0.3$ and 0.7, with three typical frequency ratios as in figure 5(b). Similar to the analysis of the results shown in figure 6, the non-periodic-flow state is observed clearly for $A = 0.3$ and $F = 0.35$ in figure 8(a) and $A = 0.7$ and $F = 0.9$ in figure 8(b). On the other hand, the periodic state is observed for $A = 0.3$ with $F = 0.7$ and 1.05 in figure 8(a) and $A = 0.7$ with $F = 1.0$ and 1.05 in figure 8(b).

4.2. *Forward and backward movements in the periodic regime*

The plate movements as a result of the fluid–plate interaction are closely related to the flapping-based locomotion of swimming and flying animals. The behaviours in the periodic regime are now discussed further. We have noticed that there exist two dynamical responses of the passively pitching plate in the periodic regime (forward or backward moment). Furthermore, we find that the moving direction depends only on the frequency ratio F.

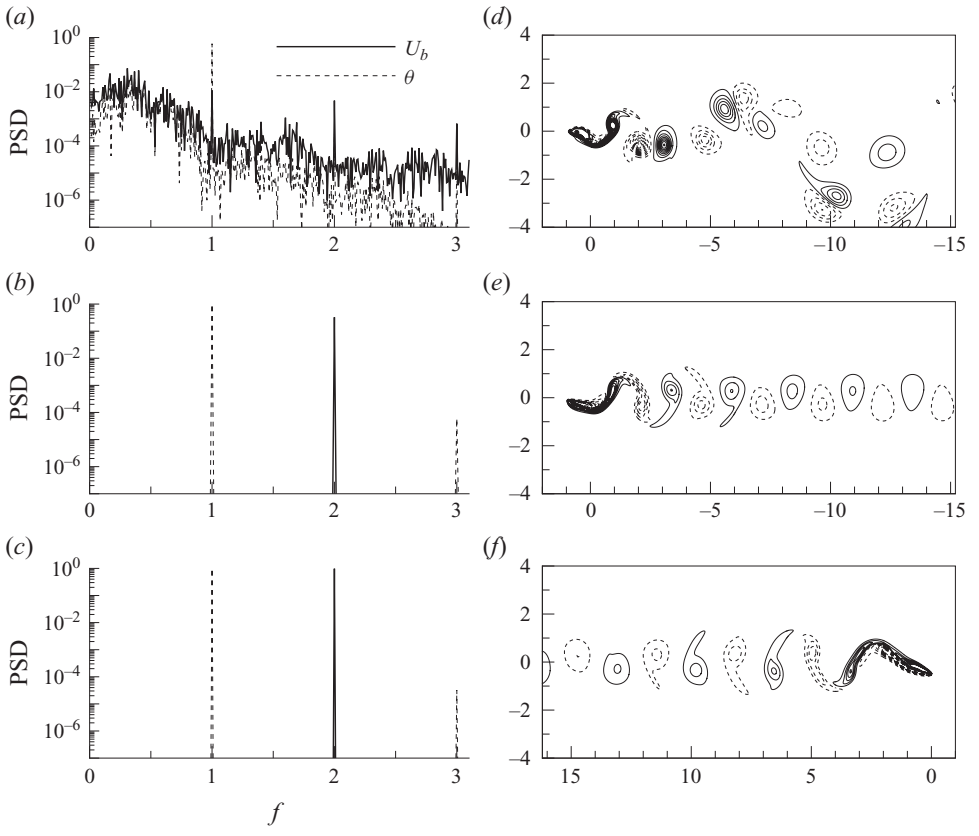

FIGURE 7. Power spectrum densities (PSDs) of the horizontal speed U_b and passive pitching angle θ exhibited in figure 6 (a–c) and the corresponding instantaneous vorticity contours (d–f) for $F = (a, d)$ 0.7, (b, e) 0.95 and (c, f) 1.05. In PSDs (a–c), solid line represents the PSD of U_b and dashed lines the PSD of θ. In vorticity contours (d–f), solid lines denote positive values and dashed lines negative values.

As typically shown in figures 6(a) and 8, we can identify that the plate lies in the backward-movement regime with $U_b(t) < 0$ or its mean value $U < 0$ after the plate reaches a steady movement (corresponding to region II with $F \leqslant 1$ in figure 5), and the plate lies in the forward-movement regime with $U_b(t) > 0$ or its mean value $U > 0$ (corresponding to region III with $F > 1$ in figure 5). On examining the evolution of vortex structures and the plate motion during the initial cycles, it is found that the moving direction of the plate can be determined after a few flapping cycles, as shown in figures 6(a) and 8, and is dependent on F, i.e. $F \leqslant 1$ for the backward movement and $F > 1$ for the forward movement. The dynamical responses found here differ from those of a symmetric wing that is flapped vertically in a fluid where the wing can move in either direction independent of the flapping frequency (Vandenberghe *et al.* 2004; Alben & Shelly 2005; Lu & Liao 2006).

We further discuss the flow behaviours in the region of small linear density ratio ($D \sim 1$) based on the results in figure 5. As β increases, the flow state may directly change from the periodic forward motion in region III to the non-periodic motion in region I. A similar switch occurs if the flapping frequency increases or F decreases.

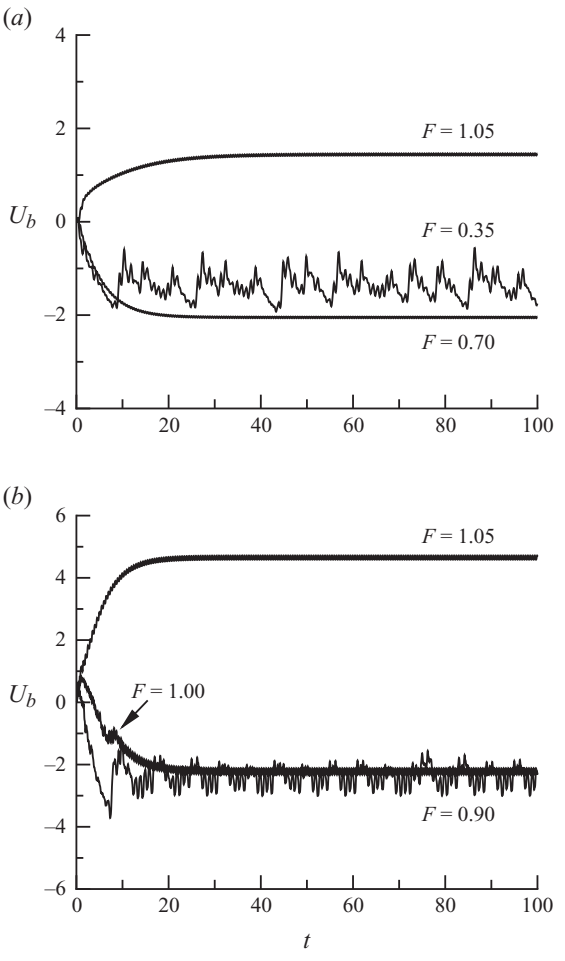

FIGURE 8. Time histories of horizontal speed U_b for three typical values of F with $\beta = 80$, $D = 2$ and $A = (a)$ 0.3 and (b) 0.7.

Thus, the dynamical phenomena found here are consistent with the experimental findings (J. Zhang, private communication, 2008).

The phase shift φ between the vertical oscillation $y_b(t)$ in (2.3) and the passive pitching motion characterized by the pitching angle $\theta(t)$ is an important parameter (e.g. Anderson *et al.* 1998; Dickinson *et al.* 1999) for understanding the mechanisms related to the forward and backward movements. Figure 9 shows the variations of $y_b(t)$ and $\theta(t)$ in one cycle for $F = 0.95$ and 1.05, corresponding to the cases in figures 6(a) and 6(b). A delayed phase shift of $\theta(t)$ with respect to $y_b(t)$ occurs in figure 9(a) for $F = 0.95$ and is associated with the backward movement, while an advanced phase shift exists in figure 9(b) for $F = 1.05$ and is associated with the forward movement.

An overview of the phase shift φ on the (φ, F) and (φ, U) planes is shown in figure 10 for the chosen parameters. Consistent with the above analysis of figure 9, we can obtain a relationship among φ, F and U, which reveals that $\varphi > 0$ corresponds to the forward movement ($U > 0$) with $F > 1$ and $\varphi < 0$ corresponds to the backward movement ($U < 0$) with $F \leqslant 1$. As the forward movement is related to the

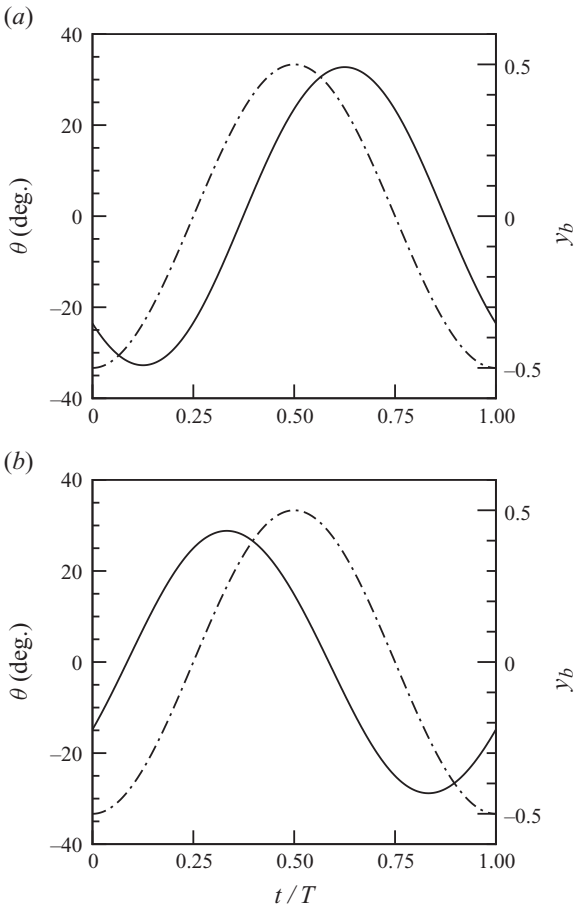

FIGURE 9. The relationship between the pitching angle θ (solid line) and the vertical movement y_b (dashed–dotted line) of the edge of the plate over one cycle after the plate reaches the steady state of movement for $\beta = 80$, $D = 2$, $A = 0.5$ and $F = (a)$ 0.95 and (b) 1.05.

flapping-based locomotion of swimming and flying animals, we will pay more attention to the underlying mechanisms in the forward-movement regime.

4.3. *Dynamical behaviours and propulsive properties*

The dynamical behaviours and propulsive properties of the passive pitching plate in the periodic regime are further analysed in terms of some typical quantities such as the mean horizontal speed, the pitching angle, the Strouhal number and the propulsive parameter for a self-propelled body.

In order to understand the effect of the frequency ratio F on the dynamical responses of the plate, figure 11 shows the mean horizontal speed and the root-mean-square (r.m.s.) value of the pitching angle (i.e. θ_{rms}) for several values of β and A. For each pair of β and A under examination in figure 11(a), the forward speed U increases as F increases from 1, reaches a maximum in the range of $F = 1.5$–3.5 (e.g. $F = 1.5$ for $\beta = 20$ and $A = 0.5$; $F = 3.5$ for $\beta = 80$ and $A = 0.7$) and approaches a constant as F increases further. The increase of F means that the spring becomes stiffer in the system (2.4). Thus, the motion of the passively pitching plate tends to the rigid case at a large value of F, e.g. $F = 10$. As an example, one may see the results for $\beta = 80$ and

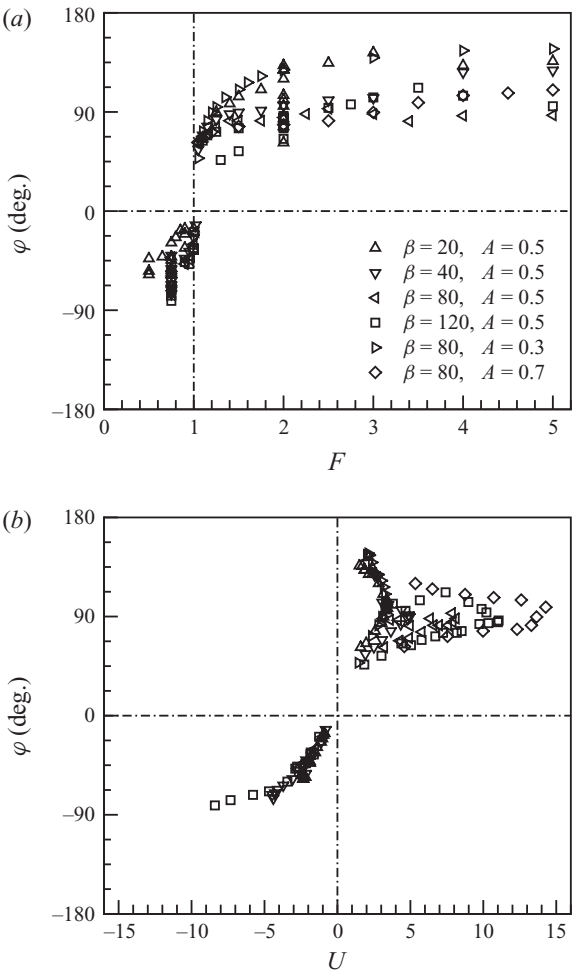

FIGURE 10. Overview of the phase shift φ versus (a) the frequency ratio F and (b) the mean horizontal speed U.

$A = 0.5$ in figure 11(a): the largest forward speed is approximately 8.12 at $F \simeq 2.25$, which is increased by 179 % with respect to the forward speed of the rigid model which is approximately 2.91. Thus, the torsional flexibility can remarkably improve the propulsive performance.

As shown in figure 11(b) for θ_{rms}, a peak occurs at $F = 1$ due to the resonance effect. Although synchronous vibration and large pitching angle occur, the plate still moves backwards at a low speed. The pitching angle decreases monotonically with the increase of F. In the range of $F = 1.5$–3.5 with relatively large forward speed, the amplitude of the pitching angle θ_m is approximately 5°–25°.

From the results in figure 11, we can further discuss the effects of β and A on the forward speed and the pitching angle. A careful examination of the results for $\beta = 20$–120 with $A = 0.5$ shows that the forward speed increases substantially and the pitching angle decreases somewhat with the increase of β. To clearly show the effect of A on the dynamical responses of the plate, as typically shown in figure 12, the case where the forward/backward speed and the pitching angle increase with A is

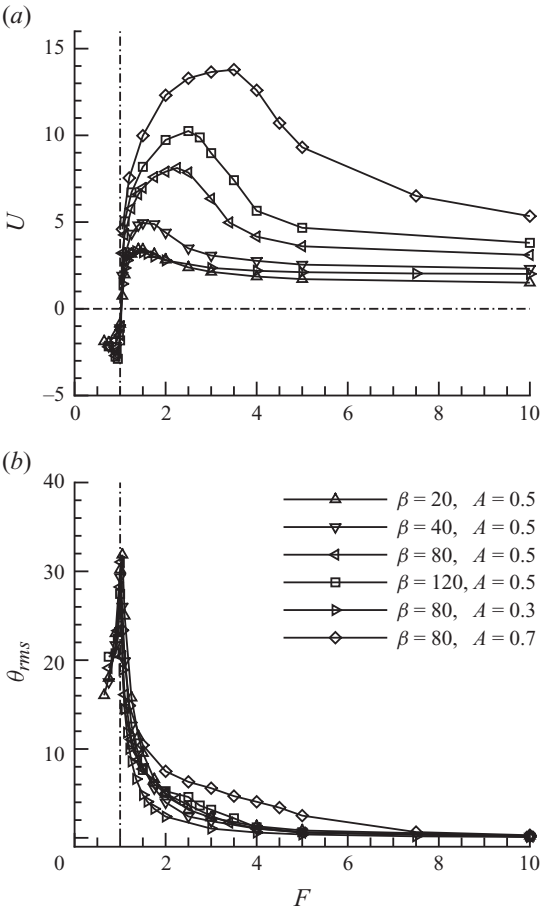

FIGURE 11. Profiles of (a) the mean horizontal speed U and (b) the r.m.s. value of the pitching angle θ_{rms} versus the frequency ratio F.

considered in this study. We would like to point out that the parameters considered here lie in the periodic regime. When A increases further for $F = 0.9$, the flow state will enter the non-periodic regime.

Figure 13 exhibits some calculated results in region III on the (Re_f, Re_U) plane. The forward Reynolds number Re_U basically increases with the flapping Reynolds number Re_f. The kinematics of the wing or tail-fin of swimming and flying animals are usually well described by the Strouhal number, which is defined as $St = A_w f/U$, where A_w is the width of the wake, assumed to be the maximum excursion of the plate trailing edge or double amplitude $A_w = 2\bar{A}$ (Triantafyllou, Triantafyllou & Gopalkrishnan 1991; Lu & Liao 2006). By the definitions of the forward and flapping Reynolds number, the Strouhal number can be expressed as $St = 2Re_f/Re_U$. As shown in figure 13, we can obtain the distribution of St. Moreover, the Strouhal number is known to describe a well-defined series of vortex growth and shedding regimes for a flapping body, which will be discussed in § 4.4 for the vortical structures.

In the forward-movement regime, the plate propels itself in the horizontal direction. We suggest that confusion that the drag and thrust cannot be separated in studies of fish swimming (e.g. Lighthill 1975; Fish 1993) arises. Consider a self-propelled ship,

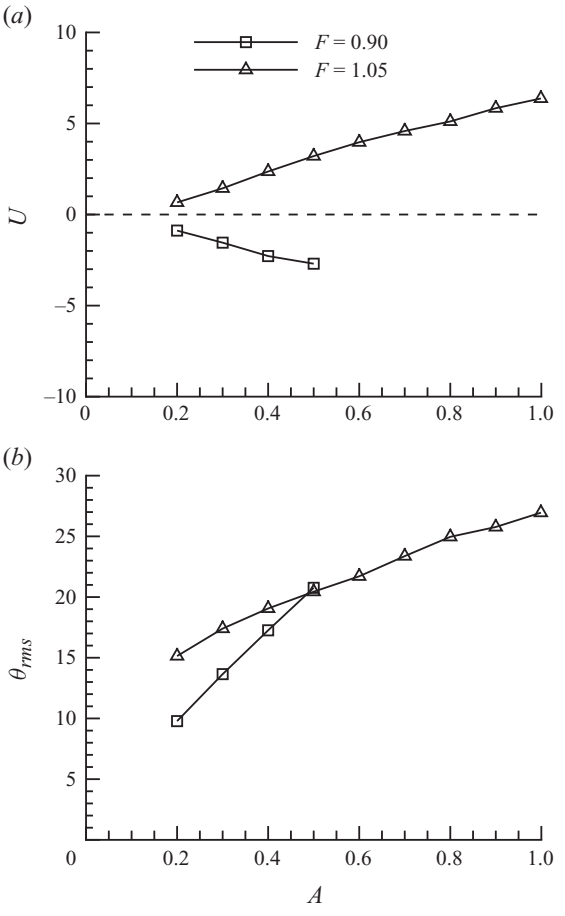

FIGURE 12. Profiles of (a) the mean horizontal speed U and (b) the r.m.s. value of the pitching angle θ_{rms} versus the flapping amplitude A for $\beta = 80$ and $D = 2$.

where thrust is attributed to the propeller and drag to the ship's body. Hence, it is reasonable to calculate the thrust and drag for the propeller. However, the thrust and drag for the 'combination' of the propeller and the ship are both zero at steady state. The spontaneous motion of the plate is such a combination (Schultz & Webb 2002). To characterize the propulsive efficiency of a self-propelled body, the ratio of the kinetic energy of the forward motion of the body and the work used by the deforming body over one undulation cycle was proposed by Kern & Koumoutsakos (2006). The amount of the work is computed as a time integral of the power output of the surface of the body on the surrounding fluid (Kern & Koumoutsakos 2006). Following their idea, we introduce a propulsive parameter defined as $f_\eta = E/W$, where $E = (1/2)m_s U^2$ and $W = \int_t^{t+T} F_y(\mathrm{d}y_b/\mathrm{d}t)\mathrm{d}t + \int_t^{t+T} T_r(\mathrm{d}\theta/\mathrm{d}t)\mathrm{d}t$, with m_s being the specific mass of the plate and F_y the vertical force component exerted on the plate.

Figure 14 shows the profiles of the forward propulsive parameter. The high propulsive parameter for several pairs of β and A under examination lies in the range of $St = 0.15$–0.35 in figure 14(a), which is consistent with the regime selected by flying and swimming animals in nature (Taylor *et al.* 2003). Similarly, corresponding

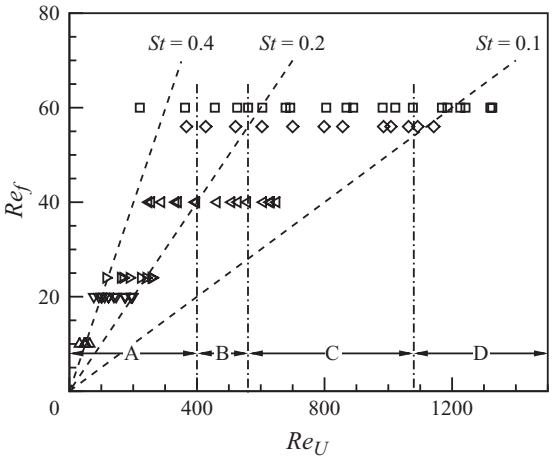

FIGURE 13. The forward Reynolds number Re_U versus the flapping Reynolds number Re_f for the plate forward movement. Symbols have the same meanings as in figure 10. Dashed lines represent the Strouhal number obtained by $St = 2Re_f/Re_U$. Regions A–D correspond to four kinds of vortex structures in the wake of the flapping plate.

to the high propulsive parameter, the phase shift is in the range $\varphi = 60°$–$90°$ in figure 14(b) and the pitching angle $\theta_m = 10°$–$25°$ in figure 14(c) may also be related to high propulsive efficiency adopted by swimming and flying animals (e.g. Ennos 1988*b*, 1989; Fish 1993). This will be discussed in § 4.5 in detail.

4.4. *Vortical structures for the forward movement*

The vortical structures in the wake are related to the propulsive properties of a flapping wing (von Ellenrieder, Parker & Soria 2003; Dong, Mittal & Najjar 2006; Buchholz & Smits 2008). The forces on the body are mainly dependent on the vortical structures near the body (Wu, Lu & Zhuang 2007). Therefore, they are discussed further here. Based on our careful examination, it is found that the vortex structures depend mainly on the forward Reynolds number Re_U and there exist four kinds of vortex structures in the near wake. The corresponding Re_U range for the vortex structures is given by the four regions (i.e. A–D) in figure 13.

The instantaneous vorticity contours for the four wake patterns are shown in figures 15(a)–15(h). When the plate moves forward, a shear layer is generated along the surface and is gradually shed into the downstream to form concentrated vortices. As shown in figures 15(a) and 15(e) for Re_U in region A, there are two vortices, with opposite signs, shed downstream during one flapping cycle. Finally, a reverse von Kármán vortex street forms in the wake of the plate. This type of vortex structure is named pattern A. Similar vortical structures behind a flapping flight foil have been observed experimentally (e.g. Vandenberghe *et al.* 2004, 2006; Godoy-Diana *et al.* 2009) and numerically (e.g. Lewin & Haj-Hariri 2003; Alben & Shelly 2005; Lu & Liao 2006).

When the plate moves with a greater speed in region B, as shown in figures 15(b) and 15(f), two vortices with the same sign are shed downstream in one half-cycle, and the other two oppositely rotating vortices are formed in the following half-cycle. Such vortical structures are seen experimentally as well in a flapping foil (Schnipper, Andersen & Bohr 2009). The two same-sign vortices coalesce when they evolve

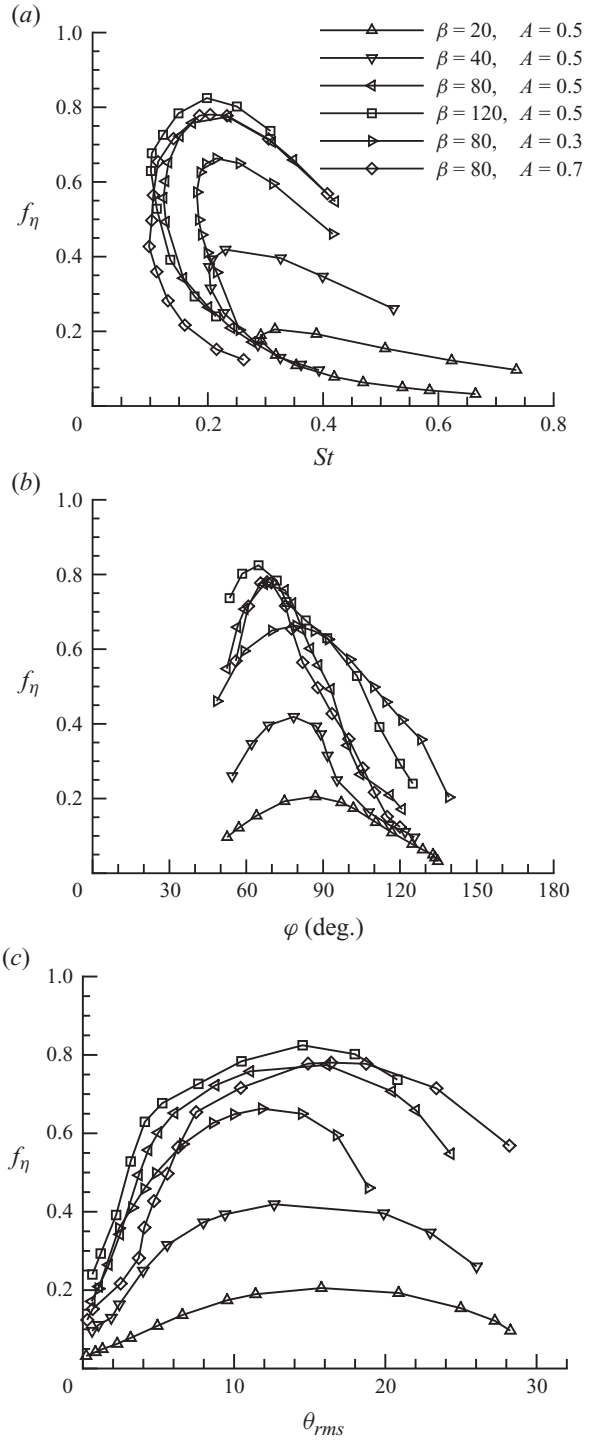

FIGURE 14. Profiles of the forward propulsive parameter f_η versus (*a*) the Strouhal number St, (*b*) the phase shift φ and (*c*) the r.m.s. value of the pitching angle θ_{rms}. The legend is the same as in figure 11.

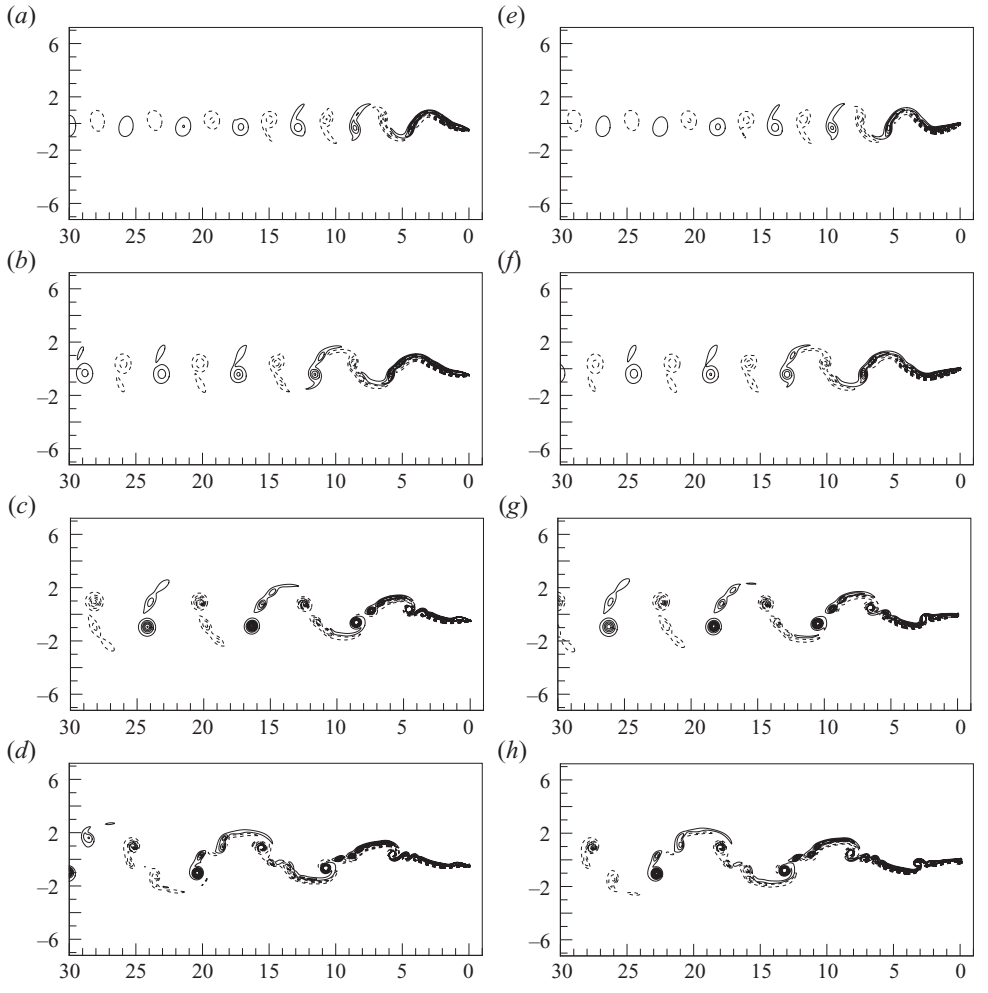

FIGURE 15. Instantaneous vorticity contours for $D=2$ and $A=0.5$ with (a, e) $\beta=80$, $St=0.235$; (b, f) $\beta=80$, $St=0.173$; (c, g) $\beta=80$, $St=0.123$; and (d, h) $\beta=120$, $St=0.098$ at $t/T=0/4$ (a–d) and $1/4$ (e–h). Solid lines denote positive values and dashed lines negative values.

downstream. In the downstream region, a reverse von Kármán vortex street develops gradually. The vortical structure is called pattern B (see figures 15b and 15f).

As the forward speed increases further, typical vortex structures are shown in figures 15(c) and 15(g), and 15(d) and 15(h), corresponding to regions C and D, respectively. The shear layer shed from the plate becomes unstable due to the Kelvin–Helmholtz instability and gradually rolls up to form a series of eddies in the near wake, which are similar to the vortex patterns for a flow past a flexible filament (e.g. Zhang *et al.* 2000; Shelley, Vandenberghe & Zhang 2005). Figures 15(c) and 15(g) exhibit that three vortices with the same sign are shed downstream per half-cycle, and this vortical structure is called pattern C. It is also observed that four or even more vortices with the same sign occur per half-cycle, which is called pattern D (see figures 15d and 15h). Farther downstream, the same-sign vortices coalesce when they evolve. As the Strouhal number St becomes smaller, e.g. in regions C and D of figure 13,

more vortices shed downstream during one cycle form complex vortex structures in the wake, which is consistent with experimental findings in the wake of a flapping foil (Schnipper *et al.* 2009).

In addition, when the parameters lie in the non-periodic regime, i.e. region I in figure 5, as typically shown in figure 7(*d*), a complex vortex pattern occurs. Furthermore, when the parameters lie in region II, the plate moves backwards and the vortical structures in the near wake are similar to those in figure 15 except that now the incoming flow is from the opposite direction.

4.5. *Connections to the flapping-based locomotion of swimming and flying animals*

Swimming and flying animals usually utilize flapping-based locomotion (e.g. Childress 1981; Blake 1983; Videler 1993; Brodsky 1994; Vogel 1994). In terms of some typical quantities (frequency ratio F, phase shift φ, pitching angle θ and Strouhal number St), we further discuss how these parameters are related to animal locomotion.

We first discuss the frequency ratio F. As F is associated with the torsional flexibility, we need to obtain the material behaviour of appendages. Ishihara *et al.* (2009) provided a method to calculate the natural frequency of the lumped-torsional-flexibility wing model. They considered the wing of a crane fly (*Tipula obsoleta*) with the Young's modulus $Es = 6.1$ GPa and a flapping frequency of 45.5 Hz. They calculated the natural frequency of the wing (148 Hz), which gave the frequency ratio $F \simeq 3.25$.

We have also estimated the frequency ratio of the wing of a dragonfly (*Aeschna juncea*) and the tail-fin of a goldfish (*Carassius auratus*) by the method used by Ishihara *et al.* (2009). Based on the morphological characteristics of the dragonfly (*A. juncea*) measured by Ellington (1984*a*,*b*), the natural frequency of the forewing or hindwing of a dragonfly is estimated as 100 Hz, and the wing's flapping frequency is approximately 36 Hz (Norberg 1975). This results in a frequency ratio $F \simeq 2.8$. For the tail-fin of the goldfish (*C. auratus*), we have measured the Young's modulus Es of the spine ray in the tail-fin by nanoindentation testing and obtained $Es = 5.23$–6.89 GPa. Thus, the natural frequency of the tail-fin is estimated as 30 Hz using the mean value of Es. The frequency of goldfish's tail-beat was measured in the range of 5–15 Hz (Richard 1958). We then have the frequency ratio $F = 2$–6.

Through the above analysis, we learn that the frequency ratio of the real wings and tail-fins in flying and swimming animals is always greater than 1, which is consistent with our result that the forward movement of a passively pitching plate must have $F > 1$ (see figure 5). Furthermore, as shown in figure 11(*a*), the large forward speed for the given flapping frequencies and amplitudes corresponds to the range of $F = 1.5$–3.5, which is in good agreement with the values obtained above for the real wings and tail-fins.

We now move on to the phase shift φ. To mimic the locomotion of tail-fins in swimming animals (e.g. Anderson *et al.* 1998; Triantafyllou *et al.* 2000), the propulsive efficiency of a harmonically oscillating foil in uniform flow was investigated experimentally. When the reference point for heave motion is at the one-third chord length from the leading edge, it was revealed that the phase shift with the optimum propulsive performance is approximately 75° (Anderson *et al.* 1998), which is consistent with our prediction that the high propulsive parameter corresponds to $\varphi = 60°$–$90°$ (see figure 14*b*).

The measurements on the kinematic data of the free flight of a dragonfly (*Anax parthenape julius*) and a damselfly (*Ceriagrion melanurum*) were performed by the local circulation method (Azuma & Watanabe 1988; Sato & Azuma 1997). Based on the

analysis of the flight performance, it was found that the phase shift φ of the flapping and feathering motion projecting onto the wing section lies in the range 70°–90°, which is considered to be optimal for efficiency at low beating frequency. Consistently, the large forward speed in figure 10(*b*) and the high value of the propulsive parameter in figure 14(*b*) exist within the range of $\varphi = 70°$–$90°$ in our study.

In addition, the phase shift φ versus the frequency ratio F in figure 10(*a*) can provide some physical insight into understanding of the tip-to-base torsion wave observed in the dipteran (e.g. *Eristalis tenax* and *Calliphora vicina*) flight (Ennos 1988*a*,*b*). The wing mass from the base to the tip of the wing becomes lighter (Ennos 1989) and the natural frequency becomes larger (Ishihara *et al.* 2009). As shown in figure 10(*a*), φ increases as F increases in region III for the given parameters. Thus, we can reasonably infer that the phase shift becomes larger from the base to the tip of the wing. This phase-shift variation along the spanwise direction occurs as the torsion wave in the three-dimensional wing identified in the dipteran flight by Ennos (1988*a*,*b*).

We now address θ_m. As discussed earlier, the range of $\theta_m = 5°$–$25°$ in figure 11 is related to large forward speed and corresponds to high propulsive parameter in figure 14(*c*). In contrast, Anderson *et al.* (1998) found that the pitching angle with optimum propulsive performance of a harmonically oscillating foil was within 15°–25°. Fish (1993) filmed the swimming motions of bottlenose dolphins (*Tursiops truncatus*) and investigated the angle between the tangent of the flukes' path and the axis of the flukes. It was found that the maximum angle of attack of the flukes ranged from 5° to 30° during cruise swimming. This is consistent with our numerical data.

Finally, we discuss the relationship between the Strouhal number St and the animal locomotion. Usually, St is referred to as an appropriate parameter governing propulsive performance. Optimal St depends subtly on kinematic parameters, including the flapping angle, the amplitude and the phase shift. For any given motion, the efficiency is higher over the range of $0.2 < St < 0.4$ (e.g. Triantafyllou *et al.* 1991; Anderson *et al.* 1998; Triantafyllou *et al.* 2000). Based on the studies of 42 species (birds, bats, insects, sharks, bony fish and dolphins) in their cruise motions (Taylor *et al.* 2003 and the references therein), the value of St was found to lie in the interval $0.15 < St < 0.5$. Within this range, the cruise of the flying and swimming animals driven by the wing or tail is likely to have high propulsive efficiency. In contrast, our present numerical studies indicate that the high propulsive parameter (see figure 14*a*) occurs for $St = 0.15$–0.35 approximately. In addition, St is also known to govern a well-defined series of vortex growth and shedding regimes for a flapping wing. With $St = 0.15$–0.35, a reverse von Kármán vortex street in the wake occurs (see figures 15*a* and 15*e*, and 15*b* and 15*f*, patterns A and B), which is associated with thrust production in animal locomotion.

5. Concluding remarks

The locomotion of a passively flapping plate has been studied using a multiblock LBM. Based on our calculations in a wide range of parameters, various aspects of the mechanics behind the behaviour of a flapping plate are investigated. Here, we briefly summarize the results obtained and discuss the mechanisms relevant to the flapping-based locomotion of swimming and flying animals.

We have found that there exist two typical flow states, i.e. a periodic- and a non-periodic-flow state in a fluid–plate system. The boundary between the two flow states

depends on the governing parameters and is determined on the (F, D) plane. The non-periodic region shrinks somewhat as the linear density ratio D increases, and expands with the increase of the frequency Reynolds number β and the flapping amplitude A.

In the periodic-flow regime, we have observed that there exist two typical dynamical responses of the passively pitching plate. Because of dynamic forces exerted on the plate by the surrounding fluid, the plate will propel itself in the horizontal direction. We have found that the movement direction depends only on the frequency ratio F, which is associated with the lumped torsional flexibility. The plate will move forwards when $F > 1$ and backwards when $F \leqslant 1$. The phase shift φ between the heaving and the passive pitching motion is an important parameter related to the forward and backward movements. Based on the numerical analysis, we have obtained that $\varphi > 0$ corresponds to the forward movement (i.e. $U > 0$) with $F > 1$ and $\varphi < 0$ corresponds to the backward movement ($U < 0$) with $F \leqslant 1$. This indicates the connection between the forward movement of the plate and the flapping-based locomotion of swimming and flying animals.

The dynamical behaviours and propulsive properties of the passively pitching plate in the forward-motion regime have been analysed in detail. The study of the effect of the frequency ratio F on the plate motion indicates that the torsional flexibility can remarkably improve the propulsive performance. Moreover, it is found that the forward speed increases with the increase in β and A for the parameters used in this study.

When the plate moves forwards, the vortex structures in the near wake depend mainly on the forward speed U or the Reynolds number Re_U. We have identified four kinds of vortex structures, i.e. patterns A–D exhibited in figure 15. The Strouhal number St is a parameter to govern a well-defined series of vortex growth and shedding regimes for a flapping wing. When $St = 0.15$–0.35 (the range found in flying and swimming animals), a reverse von Kármán vortex street (corresponding to patterns A and B) occurs which is associated with the thrust production in animal locomotion.

Finally, we have discussed the relationships between our computational results and the animal's flapping-based locomotion in terms of the frequency ratio F, the phase shift φ, the pitching angle θ and the Strouhal number St. The extensive comparison and discussion in § 4.5 indicate that our numerical results are consistent with those of the observations and measurements of swimming and flying animals.

The results obtained in this study may provide physical insight into the understanding of the propulsive mechanisms of the flapping wings and fins in swimming and flying animals. However, the flow relating to animal locomotion is certainly far more diverse and complex than the flow around the pitching plate considered here. Ideally, three-dimensional computations of viscous flows around flexible bodies are desirable. This will be a subject of our further work.

The authors are very grateful to Professor J. Zhang at New York University for the valuable discussions and Professor L. Zhu at Indiana University–Purdue University, Indianapolis, for help in improving the paper. This work was supported by the Natural Science Foundation of China (Grant no. 10832010), the Innovation Project of the Chinese Academy of Sciences (Grant no. KJCX2-YW-L05) and the 111 Project (Grant no. B07033).

REFERENCES

Aidun, C. K. & Ding, E. J. 2003 Dynamics of particle sedimentation in a vertical channel: period-doubling bifurcation and chaotic state. *Phys. Fluids* **15**, 1612–1621.

Aidun, C. K., Lu, Y. N. & Ding, E. J. 1998 Direct analysis of particulate suspensions with inertia using the discrete Boltzmann equation. *J. Fluid Mech.* **373**, 287–311.

Alben, S. & Shelly, M. 2005 Coherent locomotion as an attracting state for a free flapping body. *Proc. Natl Acad. Sci. USA* **102**, 11163–11166.

Alexander, R. M. 1993 *Principles of Animal Locomotion*. Princeton University Press.

Anderson, J. M., Streitlien, K., Barrett, D. S. & Triantafyllou, M. S. 1998 Oscillating foils of high propulsive efficiency. *J. Fluid Mech.* **360**, 41–72.

Azuma, A. & Watanabe, T. 1988 Flight performance of a dragonfly. *J. Exp. Biol.* **137**, 221–252.

Birch, J. M. & Dickinson, M. H. 2001 Spanwise flow and the attachment of the leading-edge vortex on insect wings. *Nature* **412**, 729–733.

Blake, R. W. 1983 *Fish Locomotion*. Cambridge University Press.

Brodsky, A. K. 1994 *The Evolution of Insect Flight*. Oxford University Press.

Bouzidi, M., Firdaouss, M. & Lallemand, P. 2001 Momentum transfer of a Boltzmann-lattice fluid with boundaries. *Phys. Fluids* **13**, 3452–3459.

Buchholz, J. H. J. & Smits, A. J. 2008 The wake structure and thrust performance of a rigid low-aspect-ratio pitching panel. *J. Fluid Mech.* **603**, 331–365.

Chen, S. & Doolen, G. D. 1998 Lattice Boltzmann method for fluid flows. *Annu. Rev. Fluid Mech.* **30**, 329–364.

Childress, S. 1981 *Mechanics of Swimming and Flying*. Cambridge University Press.

Combes, S. A. & Daniel, T. L. 2001 Shape, flapping and flexion: wing and fin design for forward flight. *J. Exp. Biol.* **204**, 2073–2085.

Combes, S. A. & Daniel, T. L. 2003*a* Flexural stiffness in insect wings .I. Scaling and the influence of wing venation. *J. Exp. Biol.* **206**, 2979–2987.

Combes, S. A. & Daniel, T. L. 2003*b* Flexural stiffness in insect wings. II. Spatial distribution and dynamic wing bending. *J. Exp. Biol.* **206**, 2989–2997.

Connington, K., Kang, Q. J., Viswanathan, H., Abdel-Fattah, A. & Chen, S. Y. 2009 Peristaltic particle transport using the lattice Boltzmann method. *Phys. Fluids* **21**, 053301.

Dickinson, M. H., Lehmann, F. O. & Sane, S. P. 1999 Wing rotation and the aerodynamic basis of insect flight. *Science* **284**, 1954–1960.

Dong, H., Mittal, R. & Najjar, F. M. 2006 Wake topology and hydrodynamic performance of low aspect-ratio flapping foils. *J. Fluid Mech.* **566**, 309–343.

Drucker, E. G. & Lauder, G. V. 2001 Locomotor function of the dorsal fin in teleost fishes: experimental analysis of wake forces in sunfish. *J. Exp. Biol.* **204**, 2943–2958.

von Ellenrieder, K. D., Parker, K. & Soria, J. 2003 Flow structures behind a heaving and pitching finite-span wing. *J. Fluid Mech.* **490**, 129–138.

Ellington, C. P. 1984*a* The aerodynamics of hovering insect flight. II. Morphological parameters. *Phil. Trans. R. Soc. Lond.* B **305**, 17–40.

Ellington, C. P. 1984*b* The aerodynamics of hovering insect flight. III. Kinematics. *Phil. Trans. R. Soc. Lond.* B **305**, 41–78.

Ellington, C. P., van den Berg, C., Willmott, A. P. & Thomos, A. L. R. 1996 Leading-edge vortices in insect flight. *Nature* **384**, 626–630.

Ennos, A. R. 1987 A comparative study of the flight mechanism of Diptera. *J. Exp. Biol.* **127**, 355–372.

Ennos, A. R. 1988*a* The importance of torsion in the design of insect wings. *J. Exp. Biol.* **140**, 137–160.

Ennos, A. R. 1988*b* The inertial cause of wing rotation in Diptera. *J. Exp. Biol.* **140**, 161–169.

Ennos, A. R. 1989 Inertial and aerodynamic torques on the wings of Diptera in flight. *J. Exp. Biol.* **142**, 87–95.

Fang, H. P., Wang, Z. W., Lin, Z. F. & Liu, M. R. 2002 Lattice Boltzmann method for simulating the viscous flow in large distensible blood vessels. *Phys. Rev.* E **65**, 051925.

Fish, F. E. 1993 Power output and propulsive efficiency of swimming bottlenose dolphins (*Tursiops truncatus*). *J. Exp. Biol.* **185**, 179–193.

Fish, F. E. 2004 Structure and mechanics of non-piscine control surfaces. *IEEE J. Ocean. Engng* **29**, 605–621.

Gao, T. & Lu, X.-Y. 2008 Insect normal hovering flight in ground effect. *Phys. Fluids* **20**, 087101.

Gao, T., Tseng, Y.-H. & Lu, X.-Y. 2007 An improved hybrid Cartesian/immersed boundary method for fluid-solid flows. *Intl J. Numer. Methods Fluids* **55**, 1189–1211.

Godoy-Diana, R., Marais, C., Aider, J.-L. & Wesfreid, J. E. 2009 A model for the symmetry breaking of the reverse Bénard–von Kármán vortex street produced by a flapping foil. *J. Fluid Mech.* **622**, 23–32.

Gopalkrishnan, R., Triantafyllou, M. S., Triantafyllou, G. S. & Barrett, D. 1994 Active vorticity control in a shear flow using a flapping foil. *J. Fluid Mech.* **274**, 1–21.

Ishihara, D., Horie, T. & Denda, M. 2009 A two-dimensional computational study on the fluid–structure interaction cause of wing pitch changes in dipteran flapping flight. *J. Exp. Biol.* **212**, 1–10.

von Kármán, T. & Burgers, J. 1935 General aerodynamic theory-perfect fluids. In *Aerodynamic Theory*. Julius Springer.

Kern, S. & Koumoutsakos, P. 2006 Simulations of optimized anguilliform swimming. *J. Exp. Biol.* **209**, 4841–4857.

Lallemand, P. & Luo, L. S. 2003 Lattice Boltzmann method for moving boundaries. *J. Comput. Phys.* **184**, 406–421.

Lewin, G. C. & Haj-Hariri, H. 2003 Modelling thrust generation of a two-dimensional heaving airfoil in a viscous flow. *J. Fluid Mech.* **492**, 339–362.

Lighthill, M. J. 1975 *Mathematical Biofluiddynamics*. SIAM.

Liu, H., Ellington, C. P., Kawachi, K., van den Berg, C. & Willmott, A. P. 1998 A computational fluid dynamics study of hawkmoth hovering. *J. Exp. Biol.* **201**, 461–477.

Lu, X.-Y. & Liao, Q. 2006 Dynamic responses of a two-dimensional flapping foil motion. *Phys. Fluids* **18**, 098104.

Mei, R. W., Yu, D. Z., Shyy, W. & Luo, L. S. 2002 Force evaluation in the lattice Boltzmann method involving curved geometry. *Phys. Rev.* E **65**, 041203.

Norberg, R. A. 1975 Hovering flight of the dragonfly *Aeschna juncea*. In *Swimming and Flying in Nature* (ed. Y.-T. Wu, C. J. Brokaw & C. Brennen), vol. 2. Plenum.

Peng, Y., Shu, C., Chew, Y. T., Niu, X. D. & Lu, X.-Y. 2006 Application of multi-block approach in the immersed boundary-lattice Boltzmann method for viscous fluid flows. *J. Comput. Phys.* **218**, 460–478.

Qian, Y. H., d'Humieres, D. & Lallemand, P. 1992 Lattice BGK models for Navier–Stokes equation. *Europhys. Lett.* **17**, 479–484.

Ramamurit, R. & Sandberg, W. C. 2002 A three-dimensional computation study of the aerodynamic mechanisms of insect flight. *J. Exp. Biol.* **205**, 1507–1518.

Richard, B. 1958 The speed of swimming of fish as related to size and to the frequency and amplitude of the tail beat. *J. Exp. Biol.* **35**, 109–133.

Sato, M. & Azuma, A. 1997 The flight performance of a damselfly *Ceriagrion melanurum* selys. *J. Exp. Biol.* **200**, 1765–1779.

Schnipper, T., Andersen, A. & Bohr, T. 2009 Vortex wakes of a flapping foil. *J. Fluid Mech.* **633**, 411–423.

Schultz, W. W. & Webb, P. W. 2002 Power requirements of swimming: do new methods resolve old questions? *Integr. Comp. Biol.* **42**, 1018–1025.

Shelley, M., Vandenberghe, N. & Zhang, J. 2005 Heavy flags undergo spontaneous oscillations in flowing water. *Phys. Rev. Lett.* **94**, 094302.

Spagnolie, S. E. 2008 Flapping, ratcheting, bursting, and tumbling: a selection of problems in fluid–body interaction dynamics. PhD dissertation, New York University.

Sun, M. & Tang, J. 2002 Unsteady aerodynamic force generation by a model fruit fly wing in flapping motion. *J. Exp. Biol.* **205**, 55–70.

Taylor, G., Nudds, R. & Thomas, A. 2003 Flying and swimming animals cruise at a Strouhal number tuned for high power efficiency. *Nature* **425**, 707–711.

Triantafyllou, M. S., Triantafyllou, G. S. & Gopalkrishnan, R. 1991 Wake mechanics for thrust generation in oscillating foils. *Phys. Fluids* **3**, 2835–2837.

Triantafyllou, M. S., Triantafyllou, G. S. & Yue, D. K. P. 2000 Hydrodynamics of fishlike swimming. *Annu. Rev. Fluid Mech.* **32**, 33–53.

Vandenberghe, N., Childress, S. & Zhang, J. 2006 On unidirectional flight of a free flapping wing. *Phys. Fluid* **18**, 014102.

Vandenberghe, N., Zhang, J. & Childress, S. 2004 Symmetry breaking leads to forward flapping flight. *J. Fluid Mech.* **506**, 147–155.

Vanella, M., Fitzgerald, T., Preidikman, S., Balaras, E. & Balachandran, B. 2009 Influence of flexibility on the aerodynamic performance of a hovering wing. *J. Exp. Biol.* **212**, 95–105.

Videler, J. J. 1993 *Fish Swimming*. Chapman & Hall.

Vogel, S. 1994 *Life in Moving Fluids*. Princeton University Press.

Wang, Z. J. 2000 Two-dimensional mechanism for insect hovering. *Phys. Rev. Lett.* **85**, 2216–2219.

Wang, Z. J. 2005 Dissecting insect flight. *Annu. Rev. Fluid Mech.* **37**, 183–210.

Wang, Z. J., Birch, J. M. & Dickinson, M. H. 2004 Unsteady forces and flows in low Reynolds number hovering flight: two-dimensional computational *vs* robotic wing experiments. *J. Exp. Biol.* **207**, 449–460.

Wootton, R. J. 1999 Invertebrate paraxial locomotory appendages: design, deformation and control. *J. Exp. Biol.* **202**, 3333–3345.

Wootton, R. J., Herbert, R. C., Young, P. G. & Evans, K. E. 2003 Approaches to structural modeling of insect wings. *Phil. Trans. R. Soc. Lond.* B **358**, 1577–1587.

Wu, J.-Z., Lu, X.-Y. & Zhuang, L.-X. 2007 Integral force acting on a body due to local flow structures. *J. Fluid Mech.* **576**, 265–286.

Xia, Z.-H., Connington, K. W., Rapaka, S., Yue, P., Feng, J. J. & Chen, S.-Y. 2009 Flow patterns in the sedimentation of an elliptical particle. *J. Fluid Mech.* **625**, 249–272.

Yu, D. Z., Luo, L. S, Mei, R. W. & Shyy, W. 2003 Viscous flow computations with the method of lattice Boltzmann equation. *Prog. Aerosp. Sci.* **39**, 329–367.

Yu, D. Z., Mei, R. W. & Shyy, W. 2002 A multi-block lattice Boltzmann method for viscous fluid flows. *Intl J. Numer. Methods Fluids* **39**, 99–120.

Zhang, J., Childress, S., Libchaber, A. & Shelley, M. 2000 Flexible filaments in a flowing soap film as a model for flags in a two-dimensional wind. *Nature* **408**, 835–839.

Zhang, J., Liu, N.-S. & Lu, X.-Y. 2009 Route to a chaotic state in fluid flow past an inclined flat plate. *Phys. Rev.* E **79**, 045306(R).

Zhang, J. & Lu, X.-Y. 2009 Aerodynamic performance due to forewing and hindwing interaction in gliding dragonfly flight. *Phys. Rev.* E **80**, 017302.